Title: Tunable Microfibers Suppress Fibrotic Encapsulation via Inhibition of TGFβ Signaling

*Jessica Allen†, Jubin Ryu†, Alessandro Maggi, Bianca Flores, Julia R. Greer, Tejal Desai**

J. Allen, Ph.D.
UCSF Department of Bioengineering and Therapeutic Sciences:
UCSF QB3 Box 2520
1700 4th Street Rm 204
San Francisco, CA 94158-2330
Jessica.allen@ucsf.edu
415-514-9695

J. Ryu, M.D., Ph.D.
UCSF Department of Dermatology
1701 Divisadero Street
San Francisco, CA 94115
Jubin.ryu@ucsf.edu
415-514-9695

A. Maggi
California Institute of Technology
Department of Medical Engineering
1200 E. California Blvd
Pasadena, CA 91125
maggi@caltech.edu
626-395-4127

B. Flores
UCSF Department of Bioengineering and Therapeutic Sciences:
UCSF QB3 Box 2520
1700 4th Street Rm 204
San Francisco, CA 94158-2330
biancaflores@my.smccd.edu
415-514-9695

J. Greer, Ph.D.
California Institute of Technology
Division of Engineering and Applied Science
Kalvi Nanoscience Institute
1200 E California Blvd
Pasadena, CA 91125
jrgreer@caltech.edu
626-395-4127

*T. Desai, Ph.D. (corresponding author)
UCSF Department of Bioengineering and Therapeutic Sciences:
UCSF QB3 Box 2520
1700 4th Street Rm 204
San Francisco, CA 94158-2330
Email: tejal.desai@ucsf.edu

†Co-first authors

Keywords: microtopography, myofibroblast, TGFβ, fibrotic encapsulation

Abstract

Fibrotic encapsulation limits the efficacy and lifetime of implantable biomedical devices. Microtopography has shown promise in the regulation of myofibroblast differentiation, a key driver of fibrotic encapsulation. However, existing studies have not systematically isolated the requisite geometric parameters for suppression of myofibroblast differentiation via microtopography, and there has not been *in vivo* validation of this technology to date. To address these issues, a novel lamination method was developed to afford more control over topography dimensions. Specifically, in this study we focus on fiber length and its effect on myofibroblast differentiation. Fibroblasts cultured on films with microfibers exceeding 16 μm in length lost the characteristic morphology associated with myofibroblast differentiation, while shorter microfibers of 6 μm length failed to produce this phenotype. This increase in length corresponded to a 50% decrease in fiber stiffness, which acts as a mechanical cue to influence myofibroblast differentiation. Longer microfiber films suppressed expression of myofibroblast specific genes (αSMA, Col1α2, and Col3α1) and TGFβ signaling components (TGFβ1 ligand, TGFβ receptor II, and Smad3). 16 μm long microfiber films implanted subcutaneously in a mouse wound-healing model generated a substantially thinner fibrotic capsule and less deposition of collagen in the wound bed. Together, these results identify a critical feature length threshold for microscale topography-mediated repression of fibrotic encapsulation. This study also demonstrates a simple and powerful strategy to improve surface biocompatibility and reduce fibrotic encapsulation around implanted materials.

Introduction

Chronic foreign body responses and resultant fibrotic encapsulation pose one of the primary obstacles facing implantable sensors or therapeutic delivery devices. This complication limits the lifetime of the device by impairing the flow of nutrients and analytes, as well as delivery of therapeutics into the host tissue.[1–3] Fibrotic encapsulation is initiated by fibroblast recruitment to the site of implantation. Recruited fibroblasts subsequently differentiate into myofibroblasts in response to the growth factor TGFβ, as well as to mechanical tension present in the wound space.[4,5] TGFβ activates expression of alpha smooth muscle actin (αSMA) and collagen, the major protein component of the fibrotic capsule.[5] The intracellular mechanisms involved in promotion of the myofibroblast phenotype via mechanosensing are still largely unknown, but correlate with increased actin stress fiber formation, generation of internal cellular tension, and elongated cell shape.[4] Mechanical cues have been found to regulate the TGFβ pathway in a variety of contexts, and therefore it is likely that these two types of cues interact closely to regulate myofibroblast differentiation and fibrotic encapsulation.[6–8] In fact, it is well known that compliant materials can reduce the activation of the TGFβ pathway and myofibroblast differentiation.[4,7–11] However, a method to leverage this knowledge into effective product design remains elusive.

Multiple strategies have been proposed to circumvent fibrotic encapsulation, primarily focusing on material biocompatibility and co-delivery of anti-inflammatory agents, which limit and add complexity to device design, respectively.[2,3,12] In addition, previous studies have demonstrated that topography – a cue that can directly affect cell differentiation and behavior in a variety of contexts – may also be utilized to reduce the fibrotic response.[11,13–26] One advantage of topography, especially at the micro and nanoscale, is that it could conceivably alter the surface

mechanics as perceived by cellular interaction without greatly altering the design of implanted devices on the macroscale.[27] Of particular interest to implanted devices, Kam *et al.* demonstrated that high-aspect ratio microfibers, produced by imprint lithography, reduced fibroblast proliferation and differentiation *in vitro*.[19] These high-aspect ratio microfibers may represent a method to leverage the well-documented effect of compliant materials on fibroblast behavior into a material that can be applied therapeutically or as an improvement to current designs. However, this study compared a variety of geometries without a systematic isolation of specific topographical feature dimensions (e.g. fiber height or width), making it difficult to identify the minimum necessary physical parameters that lead to knockdown of the fibrotic response via topography. Moreover, it is unknown whether this effect would be replicated *in vivo*.

In this paper, we describe a novel lamination method to create microscale fibers on the surface of a polypropylene film. This approach yields microfibers that closely match the dimensions of topography previously shown to reduce myofibroblast differentiation, but additionally allows fiber length to be independently tuned by varying the lamination rate. Fibroblasts grown on long microfiber films demonstrate a reduction in expression of myofibroblast markers, as well as components of the TGFβ pathway. Murine implantation studies demonstrate the anti-fibrotic potential of these microfiber films *in vivo*, with a dramatic reduction in collagen deposition around the implanted films, as well as alteration of the fibroblastic morphology surrounding the film. These studies introduce and validate a novel way to engineer microtopography that reduces myofibroblast differentiation and prevents fibrotic encapsulation *in vivo,* thereby offering a new technology to improve the performance and longevity of implanted biomedical devices.

Results

Microfiber geometry and stiffness are defined by a simple lamination method

To determine the effect of fiber length on fibroblast morphology, polypropylene films with 1 μm diameter microfibers of either 6 μm ("short") or 16 μm ("long") lengths were fabricated using a simple lamination method (Figure 1). Briefly, microfiber height was controlled by polypropylene lamination speed while diameter was controlled by the pore size of the negative polycarbonate template. To determine the change in surface energy with the addition of microfibers, half angle measurements were completed on each type of film. While the half angle did change with the addition of microfibers on polypropylene films, the angle is not significantly different between short and long microfiber films, suggesting addition of microfibers results in a similar shift in surface energy for the polypropylene film (Supplemental Figure 1)

Nanoindentation was used to identify the relative stiffness of the fibers under compressive load. Using a flat punch diamond nanoindenter tip with a 10 μm square cross-section, the microfibers were compressed in the G200 nanoindenter at a constant prescribed displacement rate of 10 nm/s. 12 separate sets of nanoindentations in different locations on the sample were performed. Figure 2A and B show the representative load vs. displacement data for the short and long microfiber films, respectively. The linear portion of the unloading data was used to estimate the microfiber stiffness. It is important to note that the stiffness experienced by a cell on a microfiber film depends on the deflection of the microfibers in contact with the cell. The stiffness reported here is relative to the short microfiber film. Our experiments revealed that the long microfibers were less than half as stiff as short microfibers, offering a less rigid interface for attached cells (Figure 2C).

Characteristic myofibroblast morphology and gene expression are suppressed on long microfiber films.

Murine 3T3 fibroblasts cultured on both short and long microfiber films were imaged by scanning electron microscopy (SEM) and compared to fibroblasts cultured on flat polypropylene film controls. SEM images reveal a progressive change in fibroblast morphology as fiber length increases (Figure 3A). On flat controls and short microfiber films, fibroblasts possess elongated projections that emanate from the central cell body and appear rigid. In contrast, on long microfiber films, fibroblasts are devoid of these linear projections and instead adopt a more trapezoidal, less spindled morphology. High magnification SEM images of the cellular projections reveal additional differences between flat, short, and long microfiber films (Figure 3B). On flat and short microfiber films, the cellular projections are comprised of dense, linear cytoskeletal networks. On long microfiber films, the cytoskeletal network is less prominent and loosely draped over the topography, in contrast to the dense, linear network in fibroblasts grown on short microfiber and flat films.

To determine whether the differences in morphology seen in the SEM images correlate with changes in the actin cytoskeleton, cells were stained for filamentous actin (F-actin) using rhodamine phalloidin (Figure 3C). Fibroblasts cultured on flat films form prominent stress fibers with multiple vertices along the cell perimeter, reflecting points of attachment to the substrate. In contrast, fibroblasts grown on either the short or long microfiber films have less prominent stress fibers and a more rounded cell shape with fewer vertices.

Changes in cell morphology and stress fiber formation suggest that exposure to microfiber films may alter intracellular tension generation. Phosphorylation of myosin light chain (pMLC) induces intracellular tension along actin stress fibers, and 3T3 fibroblasts were

therefore stained for pMLC after 48 hours of culture (Figure 3D). Compared to cells grown on flat films, pMLC staining in fibroblasts cultured on short or long microfibers adopts a more diffuse pattern, indicating a decrease in myosin contractile activity and internal cellular tension. Staining intensity on long and short fibers was significantly decreased compared to that on flat films (Supplemental Figure 2)

The morphological and cytoskeletal changes in fibroblasts noted above suggest myofibroblast differentiation is selectively decreased on long microfibers, most likely in response to an increase in compliance at the interface. To determine the effect of microfiber length on myofibroblast differentiation, 3T3 fibroblasts were cultured on microfiber films for 48 hours in the presence of TGFβ1 to induce differentiation toward the myofibroblast phenotype. While culture on short microfiber films had no statistically significant effect compared to flat controls, culture on long fibers reduced expression of αSMA and Col1α2 by 40% and 60%, respectively (Figure 3E and F). Expression of Col3α1 was more modestly reduced on both long and short microfiber films, reaching 20% at 48 hours (Figure 3G). Therefore, microfibers beyond a critical length seem to selectively reduce myofibroblast-specific gene expression.

Long microfibers suppress activation of the TGFβ pathway.

As TGFβ directly regulates myofibroblast gene expression, the effect of microfiber length on this signaling pathway was analyzed. Fibroblasts cultured for 48 hours on both short and long microfiber films exhibited a reduction in gene expression of TGFβ signaling components, including TGFβ1 ligand, TGFβ1 receptor 2 (TβRII), and the transcription factor Smad3 (Figure 4A). However, consistent with the expression patterns of αSMA and Col1α2, knockdown of

TGFβ signaling was most pronounced in fibroblasts cultured on long microfiber films, with a 50% or greater reduction in all TGFβ signaling genes compared to flat controls.

As Smad3 RNA expression was reduced by culture on microfiber films, Smad nuclear localization, which indicates activation of Smad by TGFβ, was assessed in 3T3 fibroblasts by immunofluorescence. After 48 hours, Smad 2/3 staining intensity is markedly decreased in short and long microfibers (Figure 4B). Compared to bright nuclear staining on flat films, fibroblasts on short microfiber films have a significant reduction in nuclear staining intensity, with small regions of focal hyperintensity that localize to the nucleoli. On long microfiber films, nuclear Smad2/3 is even further decreased and diffusely distributed, with no regions of localized intensity. Smad3 (and to a lesser extent Smad2) acts as a transcription factor to up regulate αSMA, Col1α2, and Col3α1 gene expression.[28–33] Therefore, the suppression of myofibroblast specific genes in fibroblasts cultured on long microfiber films may result from this reduction of Smad2/3 activation and nuclear localization, reducing its availability for transcriptional regulation.

Long microfiber films inhibit fibrotic encapsulation *in vivo*

The above *in vitro* experiments suggest that long microfiber films reduce myofibroblast differentiation, and therefore could reduce scar tissue production and encapsulation *in vivo*. To determine the performance of microfiber films *in vivo*, flat, short and long microfiber films were implanted subcutaneously in wild-type adult mice. At two weeks post-surgery, histologic analysis with Masson's trichrome stain shows sparser deposition of collagen (in blue), as well as a 41% reduction in the fibrotic area in wounds treated with long microfiber films (Figure 5A and B). Short microfiber films did not significantly reduce collagen deposition compared to flat

controls. Additionally, at high-power magnification, a change in fibroblast morphology within the wound bed is also observed (Figure 5A, inset photos). In wound beds treated with flat films, fibroblast nuclei adopt an elongated, spindled morphology that is classically associated with myofibroblast differentiation. In contrast, fibroblasts observed at the interface of the long microfiber films have nuclei that are much more rounded with an aspect ratio closer to 1. Nuclei at the interface of short microfiber films have an intermediate aspect ratio between that of the flat and long microfiber films (Figure 5C). These differences in morphology mirrors the changes in 3T3 fibroblast morphology seen *in vitro* via SEM and immunofluorescence.

To further assess collagen deposition around flat or microfiber films *in vivo*, immunofluorescence staining was performed (Figure 6A). Deposition of collagen I is selectively reduced by 39% at the interface of the long microfiber films, while there is no significant change in collagen III staining (Figure 6B, Supplemental Figure 3). In wound beds treated with flat and short microfiber films, high magnification images demonstrate that immunofluorescence is most intense directly above and below the pocket containing the inserted film (Figure 6C). In contrast, wound beds treated with long microfiber films have differential staining, such that intense staining for collagen I is found inferior to the film, while staining is nearly absent superior to the long microfiber film. This differential intensity is noteworthy because microfibers are only present on the superior side of the inserted film. The inferior side of the microfiber film is flat and therefore acts as an internal control, inducing a similar collagen staining intensity to that found at both interfaces of the flat film.

Discussion

We demonstrate that a specific microtopography may be used to decrease fibrotic encapsulation *in vivo* by diminishing myofibroblast differentiation via suppression of TGFβ signaling. Our versatile lamination method for microfiber fabrication allows for controllable variations in geometry by simply adjusting lamination speed or polycarbonate membrane pore size and spacing. Controlling the geometry of the presented topography allowed isolation of microfiber length for study as a regulator of myofibroblast differentiation. While the topography itself can impact fibroblast differentiation (by altering the conformation, concentration of the adsorbed proteins, and available attachment area which may in turn effect integrin engagement, filopodia formation, and myofibroblast differentiation), dramatic repression of differentiation is only observed on long microfibers, compared to relatively mild effects on short microfibers.[13,17,19,34–36] Long microfibers are most likely interpreted by the cell as an increase in compliance, as increased microfiber length presents a less stiff and more deformable interface. Therefore, the reduction in myofibroblast differentiation is likely in response to mechanosensing of a compliant material.[4,7,17,37,38] It is also likely that suppression of TGFβ signaling is in response to perceived compliance, as interaction between the TGFβ pathway and mechanosensing has been identified in numerous contexts, including mechanisms that seem to directly affect Smad activation and localization, similar to the observations described in this study.[6–8]

While wound beds treated with microfibers demonstrated a dramatic reduction in collagen deposition and fibrotic response at two weeks, it should be noted that a minor fibrotic response still developed around the microfiber film. Moreover, only one time point was investigated and a full time course to a month or more would be necessary to determine the full

effect of the microfiber films on fibrotic encapsulation. Nevertheless, the reduction in the thickness and density of the capsule surrounding the microfiber film suggests that microfibers could improve diffusion of therapeutics and analytes to and from implantable devices and may represent a viable strategy in reduction of post-operative scarring. Microfibers induce changes in nuclear morphology *in vivo* that mirror changes seen *in vitro* suggesting similar mechanisms are involved in both contexts.[15] Future work should assess the effect of microfibers on other aspects of the inflammatory response, including recruitment of macrophages and other inflammatory cells. Moreover, although previous work indicates that a similar effect can be seen on polystyrene microtopography[19], polymers other than polypropylene should be investigated to determine the optimal material for the reduction of the fibrotic response using microfibers.

Conclusions

We report a novel synthesis strategy to reproducibly create polypropylene-based microscale topography. Using this approach, we define specific geometric parameters that reduce interfacial compliance and suppress myofibroblast differentiation via inhibition of the TGFβ pathway. Additionally, we demonstrate that these microfibers can reduce fibrotic encapsulation *in vivo*, demonstrating their potential use in implantable biomedical devices to prevent encapsulation.

Experimental Section

Microfiber Film Fabrication: Microfiber films were fabricated by laminating polypropylene films into microporous polycarbonate membranes in a hot roll laminator (Cheminstruments, HL-100), as described previously (Figure 1A).[39] Briefly, polystyrene (Sigma, 182427), dissolved in toluene (10% w/v), was spin-cast on to a PET backing layer. The polystyrene was used to cap a microporous polycarbonate membrane (Millipore, ATTP04700), which was then overlaid on pre-pressed polypropylene film (Lab Supply, TF-225-4). All layers were pressed through the hot roll laminator at 20 psi and 210^{0}C. Lamination speed was used to control fiber length, with short fibers pressed at 0.7 mm/s and long fibers at 0.2 mm/s (Figure 1B). Polycarbonate and polystyrene was then etched away in two serial washes in methylene chloride for 8 minutes each. All experiments were compared to flat polypropylene film controls processed as above but without the overlaid microporous membrane. Microfiber length and diameter were measured in ImageJ from SEM images and averaged from a minimum 5 film samples. Figure 1C shows the mean and standard deviation of the fiber dimensions for representative "long" and "short" microfiber films. ANOVA analysis followed by Student Newman Keuls test was used to evaluate statistical significance.

Half Angle Measurements: The surface energy of flat and microfiber films was assessed with half angle measurements using a CAM-Plus Micro/Film Contact Angle Meter (Cheminstrucments). The half angle was measured for a droplet of approximately 20 µl of water. Three films per topography were tested, with droplets applied to three separate locations for each film. ANOVA analysis followed by Student Newman Keuls test was used to evaluate statistical significance.

Nanoindentation: Microfiber films were compressed in air using the XP module of Agilent's nanoindenter G200 with a custom-made diamond flat punch indenter tip with a 10 μm square cross-section. Compressions were performed at a constant prescribed displacement rate of 10 nm/s through a feedback loop. Approximately 12 fibers were compressed simultaneously under the flat punch to depths ranging from 30% to 90% of the lengths of the straight fibers. Two load-unload cycles were performed for each sample with a hold segment of one second at peak displacement. At least 5 tests were performed for each compression depth. ANOVA analysis followed by Student Newman Keuls test was used to evaluate statistical significance. Calculated stiffnesses were compared to the harmonic contact stiffness acquired during the experiment at the data acquisition rate of ~150 Hz to ensure full contact (Supplemental Figure 4).

Cell Culture: Murine 3T3 fibroblasts were used for all *in vitro* studies. Growth media for 3T3 fibroblasts consisted of DMEM high glucose with 10% fetal bovine serum (FBS), 1% sodium pyruvate, and 1% penicillin/streptomycin. Experiments were performed in differentiation media consisting of growth media supplemented with 5 ng/ml TGFβ1 (Peprotech, 100-21).

Scanning Electron Microscope (SEM) Imaging: To prepare cells adhered to microfiber films for SEM imaging, cells were fixed in 4% paraformaldehyde in PBS for 15 minutes at room temperature. Drying was performed in 100% ethanol with a critical point dryer (Tousimis). Samples of microfiber films with and without cells were coated with 10 nm of iridium before imaging in a Carl Zeiss Ultra 55 Field Emission Scanning Electron Microscope using an in-lens SE detector at a beam voltage of 2kV and a working distance of approximately 6 mm.

Immunofluorescence: After 48 hours of culture, cells were fixed in 4% paraformaldehyde in PBS for 15 min at room temperature, permeabilized in PBS with 0.5% Triton X-100 for 5 mins and blocked for 1 hour in 10% goat serum. Primary antibodies were diluted in PBS with 2% goat

serum and 3% Triton X-100 and incubated overnight at 4°C at the following concentrations: Smad2/3 antibody 1:400 (Santa Cruz, sc8332); pMLC 1:50 (Cell Signaling, #3671). Secondary goat anti-rabbit Alexa Fluor 488 (Invitrogen, A11034) was added at a dilution of 1:400 for 1 hour at room temperature. For F-actin staining, rhodamine phalloidin (Invitrogen, R415) was diluted to 1:800 in PBS and incubated with fixed cells for 20 min at room temperature. Nuclei were counterstained in Hoechst dye and cells were visualized using a Nikon Ti-E Microscope. Images were processed in Image J and normalized to species-matched IgG controls. All figures are representative images for three or more biological replicates.

QPCR: RNA was isolated using RNeasy column purification (Qiagen, 74104). The concentration and purity of RNA was determined using a Nanodrop ND-1000 Spectrophotometer (Thermo Scientific). Approximately 1 μg of RNA was converted to cDNA in a reverse transcription (RT) reaction using the iScript cDNA Synthesis Kit (Bio-Rad, 170-8891). Quantitative PCR analysis of each sample was performed in a ViiA 7 Real Time PCR System (Life Technologies). Forward and reverse intron-spanning primers (Supplemental Table 1) and Fast SYBR Green Master Mix (Life Technologies, 4385612) were used to amplify each cDNA of interest. Each sample was run in duplicate and all results were normalized to the housekeeping gene L19. Fold changes in gene expression were calculated using the delta-delta Ct method.[40] Figures show the mean and standard deviation for a minimum of 5 biological replicates. For statistical analysis, average expression and standard error of the mean were calculated for each condition across all biological replicates, each of which is an average of two technical replicates. ANOVA analysis followed by Student Newman Keuls test was used to evaluate statistical significance.

In Vivo Studies and Histology: 6 week-old female Swiss-Hamster mice were used for our *in vivo* studies. Mice were anesthetized with intraperitoneal Avertin. On the dorsal aspect of each mouse, two 0.6 cm incisions were made and a subcutaneous pocket was dissected using surgical microscissors. In the contralateral wounds, each mouse was implanted with either a flat control or a microfiber film, and the surgical wounds were closed with non-absorbable sutures. Two weeks after device placement, the mice were anesthetized, and both dorsal surgical sites were excised using a 0.8 cm punch biopsy. Tissue samples were fixed for 24 hours in 4% paraformaldehyde and paraffin embedded. Sections were then either stained with Masson's Trichrome stain, or deparaffinized and immunostained for collagen I and III. For immunostaining, the samples were blocked in 4% BSA, and the following antibodies were used: mouse anti-collagen I at 1:100 dilution (Santa Cruz 80565), goat anti-collagen III at 1:100 dilution (Santa Cruz 8781), anti-mouse Alexa 568 at 1:500 dilution (Invitrogen), anti-goat Alexa 488 at 1:500 dilution (Invitrogen). Fibrotic area was calculated from 19 images (7 flat controls, 5 short, and 7 long microfiber films) by drawing a region of interest around the fibrotic capsule, highlighted in blue by Masson's Trichrome stain. Nuclear aspect ratio was calculated from 19 images (7 flat controls, 5 short, and 7 long microfiber films) by measuring the long and short axis of cellular nuclei (highlighted by in purple by Trichrome stain) and dividing length by width for each measured nuclei. Collagen I and III intensity was calculated from 19 images (7 flat controls, 5 short, and 7 long microfiber films) by dividing the absolute intensity of immunofluorescence by the area of the fibrotic capsule. All measurements were performed in a blinded fashion. Immunostained images were obtained using Nikon Elements software and normalized to species-matched IgG controls. ANOVA analysis followed by Student Newman Keuls test was used to evaluate statistical significance.

Acknowledgements

The authors would like to thank R. Fearing and A. Gillies at the Berkeley Biomimetic Millisystems Lab for sharing their expertise in microscale topography and granting us access to their lamination equipment. We gratefully acknowledge use of the Carl Zeiss Ultra 55 FE-SEM and supporting equipment at SF State. The FE-SEM and supporting facilities were obtained under NSF-MRI award #0821619 and NSF-EAR award #0949176, respectively. We would also like to acknowledge B. Hann and D. Wang for their aid in development and execution of the in vivo studies. This work was funded by the National Science Foundataion (NSEC). J. R. Greer and A. Maggi gratefully acknowledge the financial support of Caltech's EAS Discovery Funds.

References

1. Jung, K. I., Lee, S.-B., Kim, J. H. & Park, C. K. Foreign body reaction in glaucoma drainage implant surgery. *Invest. Ophthalmol. Vis. Sci.* **54,** 3957–3964 (2013).

2. Dang, T. T. *et al.* Enhanced function of immuno-isolated islets in diabetes therapy by co-encapsulation with an anti-inflammatory drug. *Biomaterials* **34,** 5792–5801 (2013).

3. Santos, E., Pedraz, J. L., Hernández, R. M. & Orive, G. Therapeutic cell encapsulation: ten steps towards clinical translation. *J. Control. Release* **170,** 1–14 (2013).

4. Tomasek, J. J., Gabbiani, G., Hinz, B., Chaponnier, C. & Brown, R. A. Myofibroblasts and mechano-regulation of connective tissue remodelling. *Nat Rev Mol Cell Biol* **3,** 349–363 (2002).

5. Li, A. G. *et al.* Elevation of transforming growth factor beta (TGF b) and its downstream mediators in subcutaneous foreign body capsule tissue. *J Biomed Mater Res A* **82,** 498–508 (2007).

6. Allen, J. L., Cooke, M. E. & Alliston, T. ECM stiffness primes the TGFbeta pathway to promote chondrocyte differentiation. *Mol Biol Cell* **23,** 3731–3742 (2012).

7. Huang, X. *et al.* Matrix stiffness-induced myofibroblast differentiation is mediated by intrinsic mechanotransduction. *Am J Respir Cell Mol Biol* **47,** 340–348 (2012).

8. Wipff, P.-J., Rifkin, D. B., Meister, J.-J. & Hinz, B. Myofibroblast contraction activates latent TGF-beta1 from the extracellular matrix. *J. Cell Biol.* **179,** 1311–1323 (2007).

9. Hinz, B. The myofibroblast: paradigm for a mechanically active cell. *J Biomech* **43,** 146–155 (2010).

10. Hinz, B. Tissue stiffness, latent TGF-beta1 activation, and mechanical signal transduction: implications for the pathogenesis and treatment of fibrosis. *Curr Rheumatol Rep* **11,** 120–126 (2009).

11. Mateos-Timoneda, M. A., Castano, O., Planell, J. A. & Engel, E. Effect of structure, topography and chemistry on fibroblast adhesion and morphology. *J Mater Sci Mater Med* **25,** 1781–1787 (2014).

12. Orive, G., Tam, S. K., Pedraz, J. L. & Hallé, J.-P. Biocompatibility of alginate-poly-L-lysine microcapsules for cell therapy. *Biomaterials* **27,** 3691–3700 (2006).

13. Ayala, P. & Desai, T. A. Integrin α3 blockade enhances microtopographical down-regulation of α-smooth muscle actin: role of microtopography in ECM regulation. *Integr. Biol. (Camb).* **3,** 733–741 (2011).

14. Ayala, P., Lopez, J. I., Ph, D. & Desai, T. A. Microtopographical Cues in 3D Attenuate Fibrotic Phenotype and Extracellular Matrix Deposition : Implications for Tissue Regeneration. *Tissue Eng Part A* **16,** 2519–2527 (2010).

15. Bettinger, C. J., Langer, R. & Borenstein, J. T. Engineering substrate topography at the micro- and nanoscale to control cell function. *Angew. Chem. Int. Ed. Engl.* **48,** 5406–5415 (2009).

16. Clark, P., Connolly, P., Curtis, a S., Dow, J. a & Wilkinson, C. D. Cell guidance by ultrafine topography in vitro. *J. Cell Sci.* **99,** 73–77 (1991).

17. Dalby, M. J., Riehle, M. O., Johnstone, H., Affrossman, S. & Curtis, a S. G. Investigating the limits of filopodial sensing: a brief report using SEM to image the interaction between 10 nm high nano-topography and fibroblast filopodia. *Cell Biol. Int.* **28,** 229–236 (2004).

18. Kam, K. R. *et al.* Nanostructure-mediated transport of biologics across epithelial tissue: enhancing permeability via nanotopography. *Nano Lett* **13,** 164–171 (2013).

19. Kam, K. R. *et al.* The Effect of Nanotopography on Modulating Protein Adsorption and the Fibrotic Response. *Tissue Eng. Part A* **20,** 130–138 (2014).

20. Lam, M. T., Clem, W. C. & Takayama, S. Reversible on-demand cell alignment using reconfigurable microtopography. *Biomaterials* **29,** 1705–1712 (2008).

21. McGarry, J. P. *et al.* Simulation of the contractile response of cells on an array of micro-posts. *Philos. Trans. A. Math. Phys. Eng. Sci.* **367,** 3477–3497 (2009).

22. McNamara, L. E. *et al.* Nanotopographical control of stem cell differentiation. *J Tissue Eng* **18,** 120623 (2010).

23. Muthusubramaniam, L., Zaitseva, T., Paukshto, M., Martin, G. & Desai, T. Effect of Collagen Nanotopography on Keloid Fibroblast Proliferation and Matrix Synthesis : Implications for Dermal Wound Healing. *Tissue Eng Part A* 1–9 (2014). doi:10.1089/ten.tea.2013.0539

24. Bettinger, C. J., Kulig, K. M., Vacanti, J. P., Langer, R. & Borenstein, J. T. Nanofabricated Collagen-Inspired Synthetic Elastomers for Primary Rat Hepatocyte Culture. *Tissue Eng Part A* **15,** 1321–1329 (2010).

25. Pot, S. A. *et al.* Nanoscale Topography–Induced Modulation of Fundamental Cell Behaviors of Rabbit Corneal Keratocytes, Fibroblasts, and Myofibroblasts. *Invest Ophthalmol Vis Sci* **51,** 1373=1381 (2010).

26. Dalby, M. *et al.* Fibroblast reaction to island topography: changes in cytoskeleton and morphology with time. *Biomaterials* **24,** 927–935 (2003).

27. Harvey, A. G., Hill, E. W. & Bayat, A. Designing implant surface topography for improved biocompatibility. *Expert Rev Med Devices* **10,** 257–267 (2013).

28. Zhang, W., Ou, J., Inagaki, Y., Greenwel, P. & Ramirez, F. Synergistic cooperation between Sp1 and Smad3/Smad4 mediates transforming growth factor beta1 stimulation of alpha 2(I)-collagen (COL1A2) transcription. *J. Biol. Chem.* **275,** 39237–39245 (2000).

29. Sysa, P., Potter, J. J., Liu, X. & Mezey, E. Transforming Growth Factor- b 1 Up-Regulation by Sp1 and Smad2 Transacting Factors. *DNA Cell Biol* **28,** 425–434 (2009).

30. Verrecchia, F., Chu, M. L. & Mauviel, A. Identification of novel TGF-beta /Smad gene targets in dermal fibroblasts using a combined cDNA microarray/promoter transactivation approach. *J. Biol. Chem.* **276,** 17058–17062 (2001).

31. Hu, B., Wu, Z. & Phan, S. H. Smad3 mediates transforming growth factor-beta-induced alpha-smooth muscle actin expression. *Am. J. Respir. Cell Mol. Biol.* **29,** 397–404 (2003).

32. Gu, L. *et al.* Effect of TGF-beta/Smad signaling pathway on lung myofibroblast differentiation. *Acta Pharmacol. Sin.* **28,** 382–391 (2007).

33. Ghosh, A. K., Yuan, W., Mori, Y. & Varga, J. Smad-dependent stimulation of type I collagen gene expression in human skin fibroblasts by TGF-beta involves functional cooperation with p300/CBP transcriptional coactivators. *Oncogene* **19,** 3546–3555 (2000).

34. Margadant, C. & Sonnenberg, A. Integrin-TGF-beta crosstalk in fibrosis, cancer and wound healing. *EMBO Rep.* **11,** 97–105 (2010).

35. Reynolds, L. E. *et al.* Accelerated re-epithelialization in beta3-integrin-deficient- mice is associated with enhanced TGF-beta1 signaling. *Nat. Med.* **11,** 167–174 (2005).

36. Asano, Y., Ihn, H., Yamane, K., Jinnin, M. & Tamaki, K. Increased Expression of Integrin αvβ5 Induces the Myofibroblastic Differentiation of Dermal Fibroblasts. *Am. J. Pathol.* **168,** 499–510 (2006).

37. Hinz, B. The myofibroblast: paradigm for a mechanically active cell. *J. Biomech.* **43,** 146–155 (2010).

38. Assoian, R. K. & Klein, E. A. Growth control by intracellular tension and extracellular stiffness. *Trends Cell Biol* **18,** 347–352 (2008).

39. Lee, J., Majidi, C., Schubert, B. & Fearing, R. S. Sliding-induced adhesion of stiff polymer microfibre arrays. II. Microscale behaviour. *J. R. Soc. Interface* **5,** 845–853 (2008).

40. Livak, K. J. & Schmittgen, T. D. Analysis of relative gene expression data using real-time quantitative PCR and the 2(-Delta Delta C(T)) Method. *Methods* **25,** 402–408 (2001).

Figure Legends

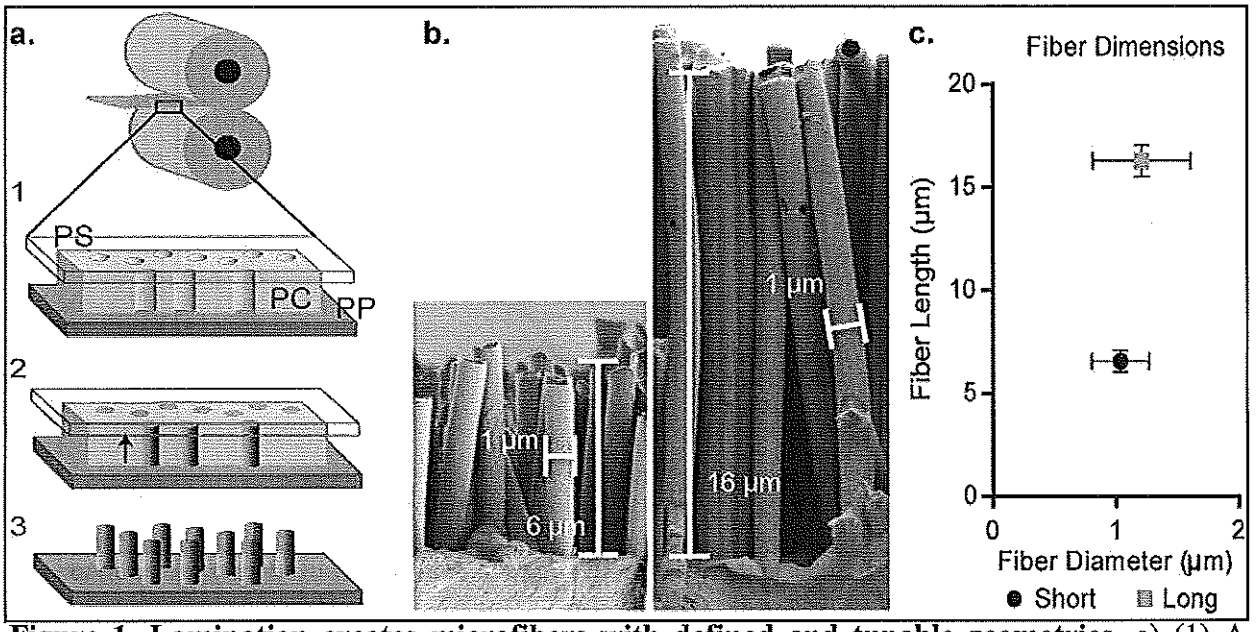

Figure 1. Lamination creates microfibers with defined and tunable geometries. a) (1) A microporous polycarbonate membrane (PC) is placed between a thin layer of polystyrene (PS) and a polypropylene film (PP). (2) The layers are pressed between two rollers at 200°C and 20 psi, melting the polypropylene film into the microporous membrane. (3) Ethylene chloride is used to etch away the polycarbonate membrane, leaving a microstructured film. b) Scanning electron microscopy images demonstrate microfiber geometry. c) Measurements of imaged microfibers reveal uniform fiber diameter and fiber length within long and short fiber films ($n \geq 5$).

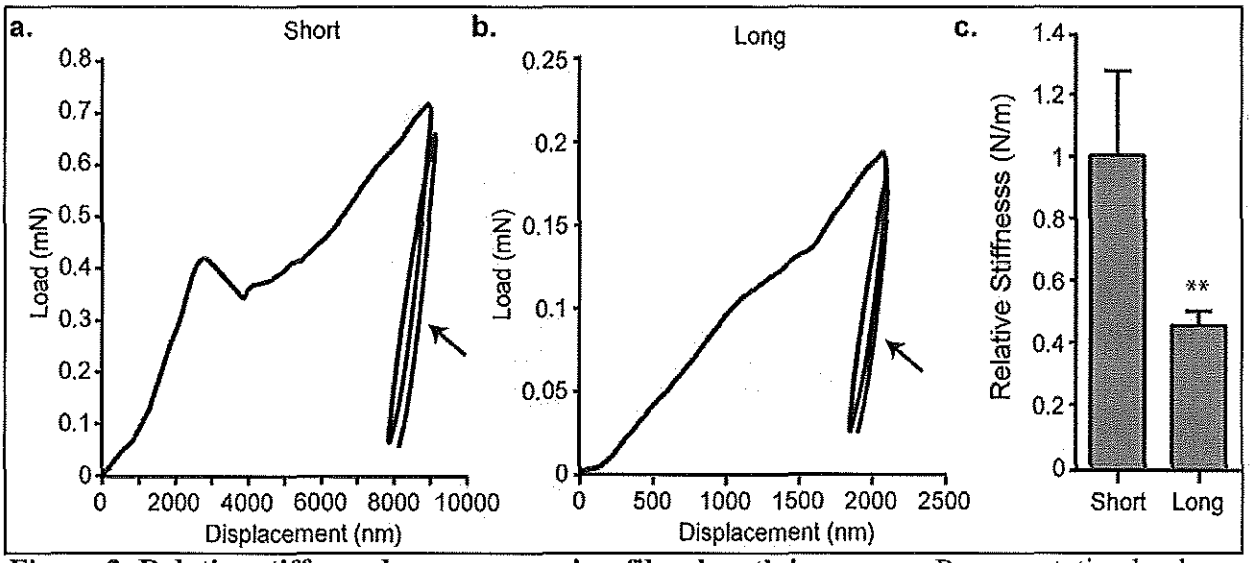

Figure 2. Relative stiffness decreases as microfiber length increases. Representative load deformation curves for the compression of short a) and long b) microfibers. Microfiber stiffness was determined from the slope of the unloading curve (arrow). c) The relative stiffness of short microfibers is twice that of the long microfibers (** $p < 0.01$, $n \geq 12$)

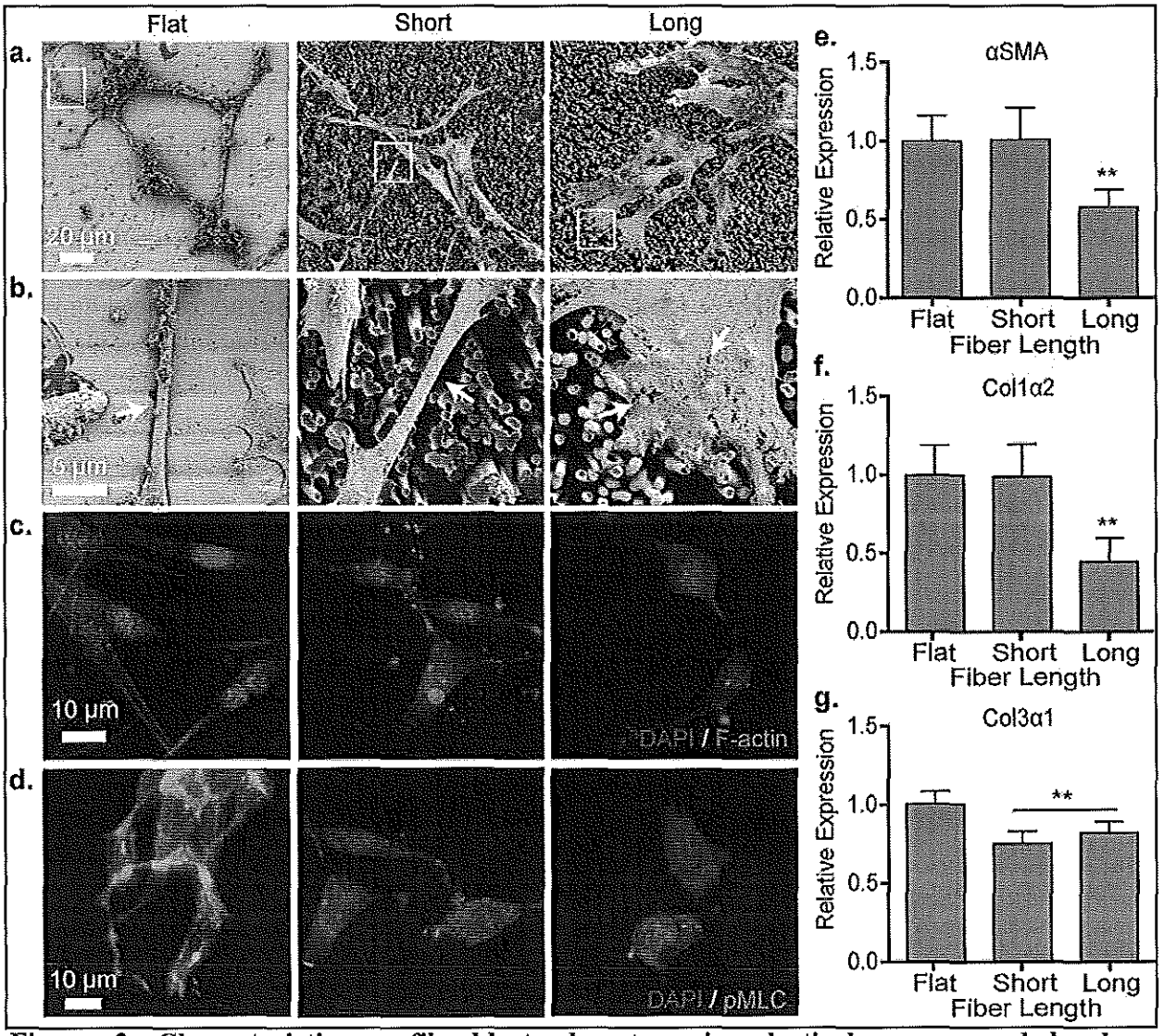

Figure 3. Characteristic myofibroblast phenotype is selectively suppressed by long microfiber films. a) Scanning electron microscopy images reveal that 3T3 fibroblasts on long (16 µm) microfibers lose the characteristic morphology and tense, linear projections classically associated with myofibroblast differentiation (n = 3). White boxes indicate areas of high magnification shown in Figure 3b. b) High magnification images of cellular projections reveal differences in cytoskeletal network density and arrangement on flat, short fiber, and long fiber films (white arrows). The linearity and density of the cytoskeleton decreases with increasing

fiber length, with the cells draped loosely over the fibers on long microfiber films. c) Rhodamine phalloidin staining of F-actin (red) reveals a loss of stress fiber formation in 3T3 fibroblasts cultured on short and long microfiber films ($n \geq 5$). d) Staining for pMLC (green) is dramatically reduced in 3T3 fibroblasts cultured on short and long microfibers compared to flat film controls ($n \geq 5$). e-g) As microfiber length increases, expression of myofibroblast-specific genes αSMA and Col1α2 progressively decreases at 48 hours. Col3α1 expression is modestly reduced on both long and short fibers ($^{**}p < 0.01$, $n \geq 5$).

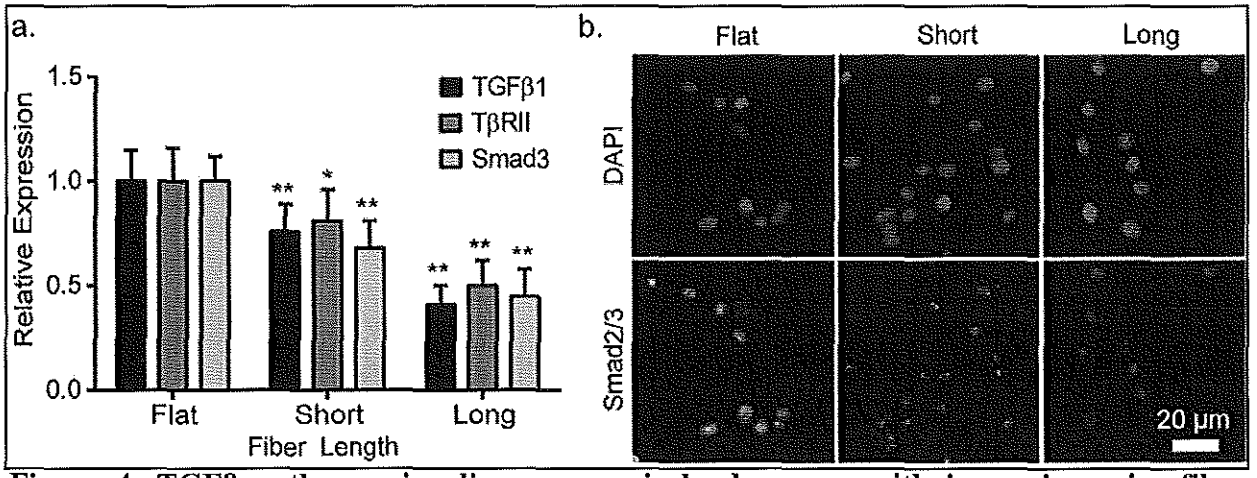

Figure 4. TGFβ pathway signaling progressively decreases with increasing microfiber length. a) As microfiber length increases, fibroblast gene expression for the TGFβ1 ligand, the receptor TβRII, and the transcription factor Smad3 are reduced. Knockdown of TGFβ signaling is most pronounced on long microfiber films. b) Similar to trends in TGFβ gene expression, Smad2/3 nuclear localization (in green) is progressively reduced as microfibers increase in length. Nuclei are marked by DAPI stain in blue ($*p < 0.05$, $**p < 0.01$, $n \geq 3$).

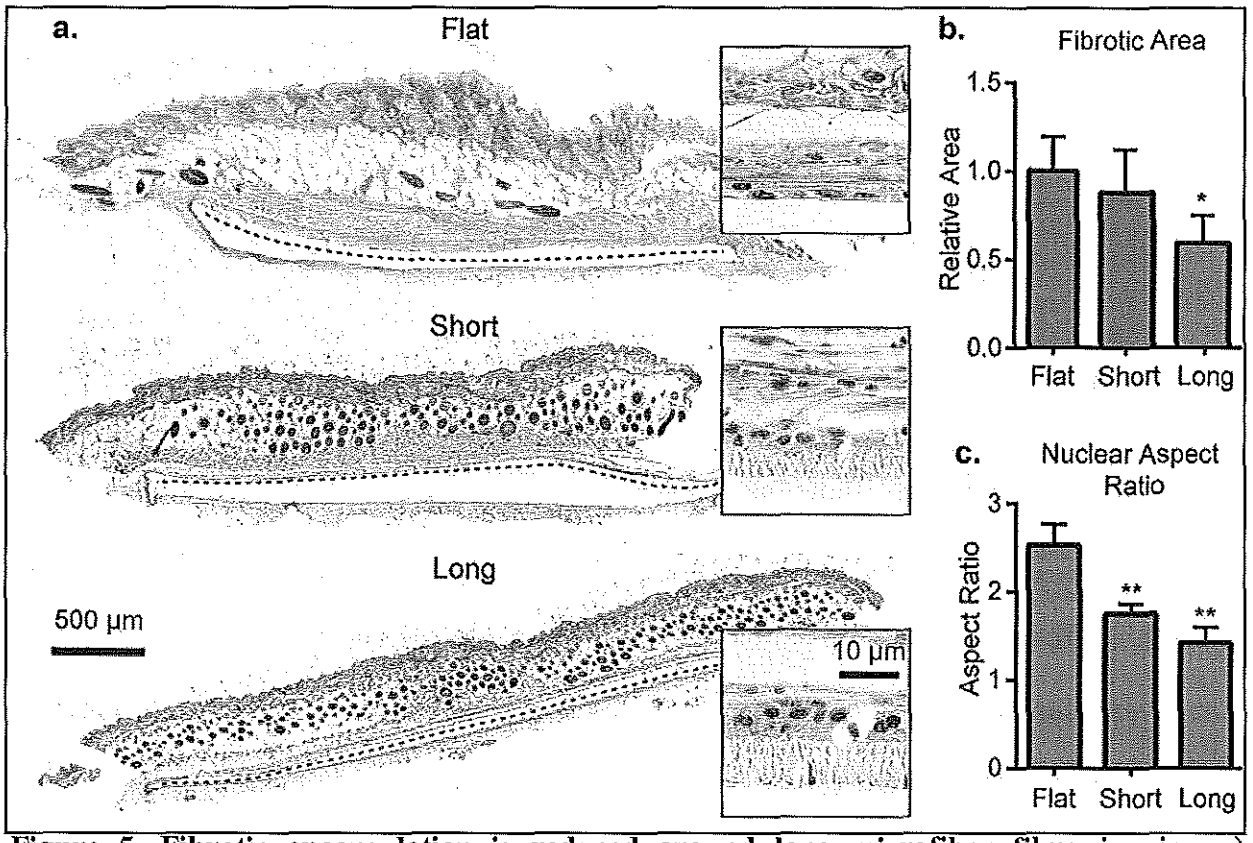

Figure 5. Fibrotic encapsulation is reduced around long microfiber films *in vivo*. a) Trichrome-stained histological sections demonstrate a decrease in collagen-rich regions (blue) around first short and then long microfiber films compared flat controls (black dashed line marks film location). Higher magnification images reveal that fibroblast nuclei adjacent to the film interface become progressively rounder on first short and then long microfiber films, in contrast to classic spindle-shaped fibroblasts found at the flat film interface (inset photos). b) Quantification of fibrotic area reveals a 41% decrease in collagen deposition around the microfiber films relative to flat controls. c) Quantification of nuclear aspect ratio demonstrates that nuclei in proximity to long microfiber films are more rounded compared to nuclei near flat controls, which are more elongated and spindled. Nuclei in proximity to short microfiber films have an intermediate aspect ratio ($*p < 0.05$, $**p < 0.01$, $n \geq 5$).

29

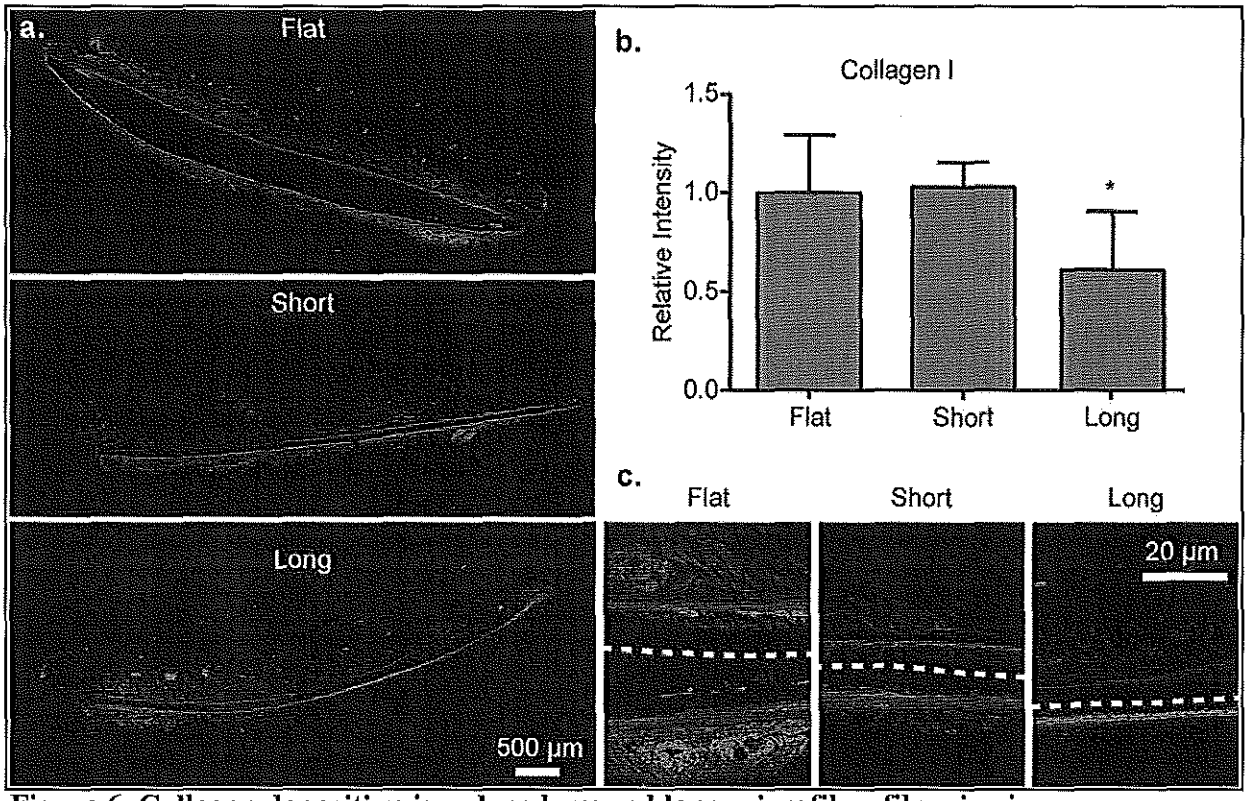

Figure 6. Collagen deposition is reduced around long microfiber films *in vivo*.

a) Immunofluorescent staining for collagen reveals a reduction in collagen I deposition around long microfiber films compared to short microfiber films and flat controls. b) Deposition of collagen I, as quantified by staining intensity, is significantly decreased above long microfiber films. c) Higher magnification images demonstrate that collagen deposition is not uniform around long microfiber films, as it is around short microfiber films and flat film controls (white dashed line). Collagen I staining is absent in the tissue exposed to the superior, long microfiber-presenting side of the film, contrasting with intense staining in the tissue exposed to the flat inferior side of the film ($*p < 0.05$, $n \geq 5$).

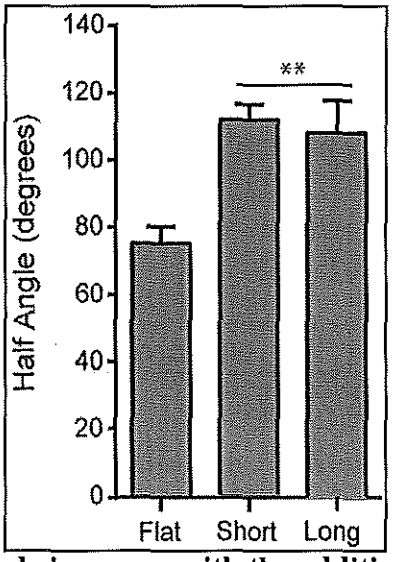

Supplemental Figure 1. Half angle increases with the addition of microfibers. Compared to half angle measurements on flat polypropylene films, the half angle increased similarly on both short and long microfiber films (**$p < 0.01$, $n \geq 3$).

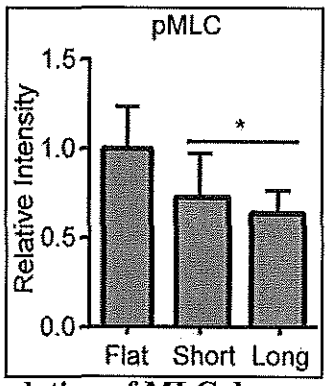

Supplemental Figure 2. Phosphorylation of MLC decreased on microfiber films.

Compared to flat controls, staining intensity for pMLC is decrease in fibroblasts cultured on long and short microfiber films (*$p < 0.05$, $n \geq 6$)

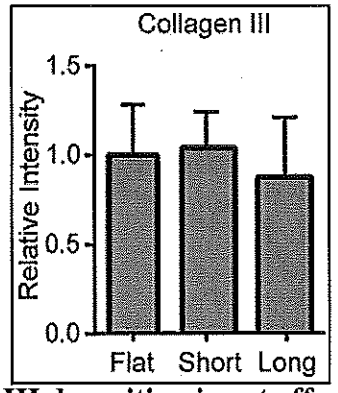

Supplemental Figure 3. Collagen III deposition is not effected by film surface. Staining intensity for collagen III is similar around flat, short, and long microfiber films. ($n \geq 5$)

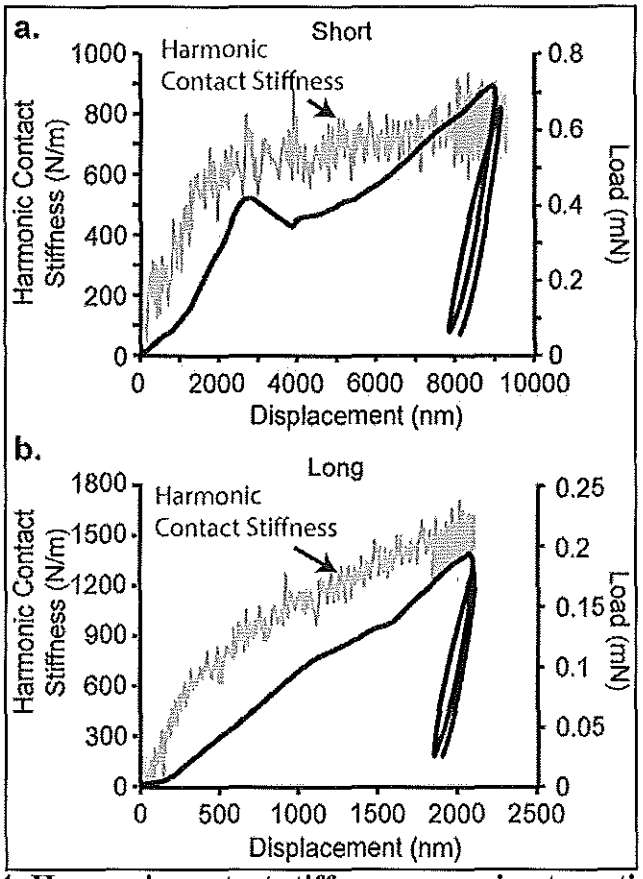

Supplemental Figure 4. Harmonic contact stiffness approximates estimated stiffness values. Harmonic contact stiffness values for both a) short and b) long microfiber films approach stiffness values for each film calculated from the linear portion of the unloading curve.

Gene	Sequence	
αSMA	F	GCTGCTCCAGCTATGTGTGA
	R	CCATTCCAACCATTACTCCCTGA
Col1α2	F	AAGGGTGCTACTGGACTCCC
	R	TTGTTACCGGATTCTCCTTTGG
Col3α1	F	CTGTAACATGGAAACTGGGGAAA
	R	CCATAGCTGAACTGAAAACCACC
TGFβ1	F	AGCCCGAAGCGGACTACTAT
	R	TCCCGAATGTCTGACGTATTG
TβR2	F	ACGTTCCCAAGTCGGATGTG
	R	TGTCGCAAGTGGACAGTCTC
Smad3	F	AAGGCGACACATTGGGAGAG
	R	GGGCAGCAAATTCCTGGTTG
rpL19	F	CATTTTGCCCGACGAAAGGG
	R	GATCTGCTGACGGGAGTTGG

Supplemental Table 1. Sequences of RT-PCR Primers